J. Comput. Appl. Res. Mech. Eng. Vol. 10. No. 2, pp. 291-309, 2021 *DOI: 10.22061/jcarme.2019.4297.1518*

Journal of Computational and Applied Research in Mechanical Engineering

jcarme.sru.ac.ir

SRTTU

JCARME

ISSN: 2228-7922

Research paper

Multi-objective particle swarm optimization of WEDM process parameters for inconel 825

P. Kumar[a,*], M. Gupta[a] and V. Kumar[b]

[a]*Department of Mechanical Engineering, National Institute of Technology, Kurukshetra, India*
[b]*Department of Mechanical Engineering, UIET, Maharishi Dayanand University, Rohtak, India*

Article info:

Article history:

Received: 23/10/2018
Revised: 27/05/2019
Accepted: 29/05/2019
Online: 02/06/2019

Keywords:

WEDM,
Inconel 825,
Surface roughness,
Wire wear ratio,
RSM,
MOPSO algorithm.

[*]Corresponding author:
nain.pawan2@gmail.com

Abstract

With the increased diversity of the customer demand and complexity of the product, Inconel 825 is widely used to meet the actual needs, especially in the aerospace industry. It is difficult-to-cut material because of its high toughness and hardness. The present research attempts to optimize the process parameters of wire electric discharge machining during the cutting operation of Inconel 825. The wire electric discharge machining characteristics such as pulse-on time, pulse-off time, spark gap voltage, peak current, wire tension, wire feed are taken into consideration. The performance was measured in terms of material removal rate, surface roughness, and wire wear ratio. The central composite design of response surface methodology at an α value of ± 2 was employed to establish the mathematical model between process parameters and performance measures. A multi-objective particle swarm optimization algorithm has been used to find the optimal solutions called Pareto optimal solutions. It uses the concept of dominance to find the non dominated set in the entire population and the crowding distance approach to finding the best Pareto optimal solutions with a good diversity of objectives. The confirmation experiments of the multi-objective particle swarm optimization algorithm show a significant improvement in material removal rate (27.934 to 31.687 mm^2/min), surface roughness (2.689 to 2.448μm), and wire wear ratio (0.027 to 0.030). SEM micrograph studies showed the number of cracks, pockmarks, craters, and pulled out material on the workpiece and wire electrode surface. Energy Dispersive X-ray analysis is performed to investigate the presence of elements on the work surface other than the base material.

1. Introduction

Nickel-based superalloys are complex materials which are diverse in demand in technologically advanced aerospace industries for manufacturing of engine components. Scientists and technologists have long relied upon high strength temperature resisting material such as Inconel and Waspaloy because of high-temperature corrosion resistance, oxidation

resistance, and creep resistance properties [1]. Among the various Inconel series, Inconel 825 possesses superior mechanical properties, provides resistance to chloride pitting as well as resistance to a variety of oxidizing atmospheres than other Inconel alloys [2]. Inconel 825 has been identified with atomic number 28 and mass number 56. With the addition of chromium and/or aluminum, the surface strength of nickel is getting improved [3] and some elements such as phosphorus, sulfur, silicon, nitrogen, and oxygen must be controlled through appropriate melting practices [4]. Inconel 825 is difficult to machine with conventional method because conventional processes are unsatisfactory and uneconomical due to hard material of tool and direct contact between tool and workpiece [5]. Besides, Inconel 825 has a tendency to weld to the cutting tool during machining, which causes tool failure [6]. Moreover, high abrasive particles in its microstructure, during machining and formation of built-up edges (BUE), makes it more difficult to machine [7].

Wire electric discharge machining (WEDM) is a non-traditional method that provides the highest degree of dimensional accuracy and surface finish for machining of high strength and temperature resistive material. It works on the spark erosion principle, in which spark is generated in discrete form in the gap (0.025 mm to 0.5 mm) between wire and workpiece. Thus, the elements are migrated due to the melting of the material from workpiece the surface [8]. The performance characteristics of WEDM is measured in terms of material removal rate (MRR), surface roughness (SR), and wire wear ratio (WWR), which are influenced by numerous machining characteristics such as pulse-on time (T_{on}), pulse-off time (T_{off}), peak current (IP), gap voltage (SV), wire tension (WT), and wire feed (WF) [9]. For achieving the optimal machining performance, i.e., higher MRR, lower SR, and WWR, proper selection of these input variables is done based on the pilot experimentation or handbook values. Moreover, the final performance of the machined product is required to determine by the analysis of surface integrity. Surface integrity viz. surface roughness, residual stress, microstructure, heat-affected zone, and microcracks were crucial in determining the final performance of the machined specimen [10].

Among the nickel-based superalloys, many reports have been published on the WEDM of the Inconel series. Goyal [11] investigated that T_{on}, tool electrode, and current intensity were the prominent factors of WEDM that affects the MRR and SR during machining of Inconel 625. Talla and Gangopadhyay [12] showed that the surface integrity of Inconel 625 is getting improved by the addition of silicon powder in dielectric when compared to the pure dielectric. Kumar et al. [13] employed Response surface methodology (RSM) based desirability approach to optimize the machining process of powder mixed electric discharge machining on Inconel 800. An optimal combination of parameters was obtained, i.e., 0.98 μs T_{on}, 0.03 μs T_{off}, 1 amp current, tool material 0.31, and the powder (suspended particles) 0.64. Bharti et al. [14] optimized EDM parameters with controlled elitist NSGA. Artificial neural network (ANN) with backpropagation was used to find the difference between experimental and ANN's predicted value. Saha et al. [15] proposed hybridization of radial basis function network (RBFN) and non-dominated sorting genetic algorithm (NSGA-II). The proposed technique was used to optimize the WEDM responses during the machining of 5 % titanium carbide (TiC) reinforced austenitic manganese steel metal matrix composite (MMC). 100 non-dominated solutions were acquired by the utilization of this technique, which resulted in remarkable enhancement of cutting speed value. Sonawane et al. [16] executed the multi-objective optimization of WEDM on Nimonic-75 alloy by utilizing Taguchi's L27 methodology combined with Principal component analysis (PCA). The results depicted that the T_{on} is the leading contributing factor (52.89%) that affected the performance measures.

Ishfaq et al. [17] evaluated the cutting performance in terms of the cutting speed of WEDM. RSM-based GRA was used to optimize the MRR, SR, and kerf width simultaneously for machining of HSS M2 grade steel. The projected combination of input parameters ensured that about 20%

enhancement of cutting speed of WEDM on stainless-clad steel. Kennedy and Eberhart [18] introduced a multi-objective optimization technique (PSO) based on swarm intelligence to find the optimum process parameters for best responses. Baskar et al. [19] compared the PSO approach with other non-traditional techniques *viz.* genetic algorithm, tabu search, ant colony algorithm and found that PSO algorithm is the most effective multi-objective optimization method for EDM process parameters optimization. Majumder et al. [20] presented a desirability-based PSO technique for optimization of EDM process parameters while machining AISI 316LN Stainless steel. Rajyalakshmi [21] optimized WEDM parameters using multi-objective PSO for machining of Monel 400. At the optimum setting of WEDM parameters, there was a 5.733% decrease in surface roughness and an 18.259% increase in MRR. Sharma et al. [22] used an RSM-based PSO approach to optimize the machining parameters of WEDM for Inconel 706. RSM with backward elimination approach was used to develop the mathematical models for cutting speed (CS) and surface roughness (SR). The experimental results revealed that the RSM based PSO approach is comparatively convenient and easier to estimate the WEDM performance attributes.

The literature review suggested that very few authors revealed the parametric optimization of WEDM for Inconel series (superalloy) using multi-objective PSO so far. Moreover, despite much higher resistance to corrosion by Inconel 825, very few studies are there which show the machining and effect of machining characteristics on the surface texture of machined Inconel 825. Hence, this research focuses on the optimization of machining characteristics of WEDM using Inconel 825 to meet the manufacturing requirements. A suitable modeling and optimization technique, RSM, is used to establish the relationship between performance characteristics and controllable input parameters. T_{on}, T_{off}, SV, IP, WT, and WF are used as machining parameters, and MRR, SR, and WWR are the performance characteristics. The developed model is used further as the fitness function for PSO, and optimum machining parameters are found.

2. Experimentation details

2.1. Work and tool material

Inconel 825 (15 cm × 15 cm × 1 cm) opted as the work material, and brass wire (250 µm) was used as the tool electrode for the present study. The chemical composition of Inconel 825 is listed in Table 1. Brass wire is made of zinc (Zn) and copper (Cu), in which the proportion of Zn is much less than Cu.

2.2. Machining setup

Experiments were performed using sprint cut computer numerical controlled (CNC) Wire Electrical Discharge Machine (WEDM). The workpiece was mounted with the help of a fixture on the machine table that can move in the x-y plane. Wire (brass wire) was fed through the workpiece continuously by a microprocessor. The upper head, which can move in the u-v axis, supplied the fresh wire under tension through the workpiece, and the lower head received the used wire. After machining of each specimen, rolled wire was extracted from the periphery of the wheel for every run to calculate the wire wear ratio. A suitable void of 25 - 500 µm was retained between the wire and the workpiece known as the plasma zone where the spark was at its highest peak. When a suitable gap voltage reached the breakdown voltage, a temperature of about 8000-10000°C was developed in the smallest gap where plasma zone occurs, as shown in Fig. 1. The elimination of matter from the workpiece was carried out by thermoelectric erosion due to ions and electrons displacement. During machining, the debris produced by the thermal erosion process was flushed by the dielectric fluid (deionsed water) continuously fed through upper and lower nozzles to the sparking area.

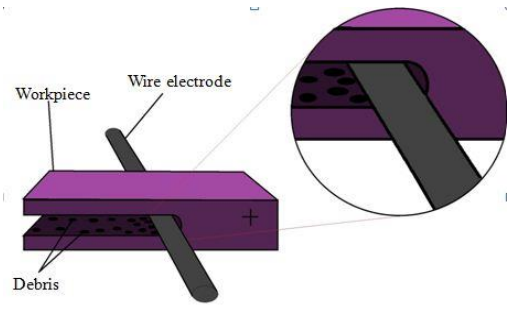

Fig. 1. Mechanism of metal removal from the work surface in WEDM.

Table 1. Chemical composition of Inconel 825.

Element	Content (wt.%)
Ni	38-46
Fe	22
Cr	19.5-23.5
Mo	2.5-3.5
Cu	1.5-3.0
Ti	0.6-1.2
C	0.05 max
P	0.02 max
S	0.03 max
Mg	1.0 max

2.3. Ranges of input and output parameters

Six variables affecting machine performance *viz.* pulse on time (A), pulse off time (B), gap voltage (C), peak current (D), wire tension (E), and wire feed rate (F) were decided for optimization of WEDM. Pilot experimentation was performed by considering 'One variable at a time' (OVAT). The values of input variables were decided by taking the results of pilot experimentation into consideration. The coded and actual values of the variables are shown in Table 2. The variables executing response *viz*. shape and size of the product (rectangular), dielectric temperature (28ºC), dielectric conductivity (20 Ω^{-1}), workpiece thickness (1.5 cm), pulse peak voltage setting (110 V), servo feed setting, wire type (brass wire of 250 µm diameter) and angle of cut (vertical) were kept constant.

2.4. Experimental procedure

A program was written in CNC code (machine language) for which a square (5 mm × 5 mm) was designed and fed through the control panel of the machine. A workpiece of 5 mm × 5 mm × 10 mm was cut from the work material by the WEDM process, and machining performances were measured in terms of MRR, SR, and WWR. During experimentation, it was reported that due to constant wire diameter the kerf width varies negligibly. Consequently, the MRR was calculated by taking Eq. (1) into consideration:

$$\text{MRR } (\text{mm}^2/\text{min}) = \text{cutting speed (mm/min)} \times \text{thickness of material (mm)} \text{ [23, 24]}.. \quad (1)$$

The cutting speed (mm/min) was displayed on the control panel of the machine, and the time taken for machining of the work material was noted down for every run. The SR of the cut specimen was measured in µm using Accretech's surfcomflex instrument SJ-301. The least count of the instrument used was 0.8 mm. A sampling length of 5 mm was selected for measurement. WWR was measured using initial wire weight and used wire weight as per Eq. (2):

$$\text{WWR} = \frac{\text{Initial wire weigh} - \text{Used wire weight}}{\text{Initial wire weigh}} \quad (2)$$

The used wire weight for one specimen was directly measured using the weighing machine. The least count in the weighing machine used was 0.02 g. The fresh wire weight used for one specimen was measured by calculating the length of the used wire. One meter length of fresh wire was 0.400 mg. The fresh wire weight was obtained by multiplying the length of the used wire by the the weight of the one-meter fresh wire.

2.5. RSM-based modeling of experiments

RSM is an assortment of mathematics helpful for developing, improving, and optimizing processes. The most extensive applications of RSM are to minimize variability in the output response of a product or to process around a target value. Central composite design (CCD) at α value of ± 2 was selected using Design Expert software (version 9.0.7, Statease Inc., Minneapolis, USA) to optimize the levels of essential variables. A total of 52 experiments were conducted, as suggested by the software, and response data was fed and analyzed by ANOVA.

Table 2. Input variables for response surface methodology.

S. No.	parameter	Unit	Level 1 (-2)	Level 2 (-1)	Level 3 (0)	Level 4 (1)	Level 5 (2)
1	T_{on}	MU*	107	109	111	113	115
2	T_{off}	MU	32	35	38	41	44
3	SV	V**	42	46	50	54	58
4	IP	A***	110	120	130	140	150
5	WT	MU	8	9	10	11	12
6	WF	m/min	4	5	6	7	8

*Machine unit, **Volt, ***Ampere

RSM based multi-objective particle swarm optimization algorithm was utilized to optimize the WEDM characteristics. A second-order polynomial equation (Eq. (3)) was employed to fit the data:

$$y=\beta_0+\sum_{i=1}^{k}\beta_i X_i+\sum_{i=1}^{k}\sum_{j=1,\ i<j}^{k}\beta_{ij}X_iX_j+\sum_{i=1}^{k}\beta_{ii}X_i^2+\varepsilon \quad \ldots \quad (3)$$

where,
y = predicted response (MRR, SR, and WWR);
x_i, x_j = independent variables;
β_0 = intercept coefficient;
β_i = regression coefficients of zero order;
β_{ij} = squared coefficients.

The performance of the model was examined by coefficient of determination R^2.

2.6. Single response optimization with PSO

PSO method is primarily based on the movement of a swarm in directional space. In the field of machine learning, it is used to find the optimum solution. In each i^{th} particle, there is a candidate solution that is represented by its velocity (v_i) and position (x_i). Particles transit from one position to another in multi-dimensional space (d) by flying. By changing its velocity, a new position of the particle arises, i.e., x_i= (x_{i1}, x_{i2}...x_{id}). In each iteration, the particle adjusts its position according to its own best position (p_{best}) and global best position (g_{best}), i.e., the experience of neighboring particles. Therefore, a new velocity value for each particle was calculated based on its current velocity. The modified velocity value was used to compute the next position of each particle in multi-dimensional space. This procedure was repeated a number of times for updating the velocity and position until a minimum error was achieved. The following steps were used in the PSO algorithm:

Step 1. Randomly design the initial population of the particles (x) over multi-dimensional space (d).
Step 2. For each particle, the objective function value is calculated.
Step 3. For each particle, find out the best position visited so far. Let it be p_{best}. Also find out the leading position of any particle in the population, i.e., $g_{best.}$
Step 4. Find the modified velocity of each particle using Eqs. (4 and 5).

$$v_{id}^{j+1}=w\times v_{id}^{j+1}+c_1\times r_1\left(pbest_i-x_{id}^{j}\right)+c_2\times r_2 \times\left(gbest_i-x_{id}^{j}\right) \quad \ldots(4) \quad (4)$$

$$w=w_{max}-\frac{w_{max}-w_{min}}{iter_{max}}\times j+1 \quad \ldots \quad (5)$$

where, c_1 and c_2 are the constant; r_1 and r_2 are random integer in the range of 0-1, w is the inertia weight, j is the iteration number, and $iter_{max}$ is the maximum number of iterations.

Step 5. Update particle's current position using Eq. (6) if the position of each particle is better than its previous best positions.

$$x_{id}^{j+1}=x_{id}^{j}+v_{id}^{j+1} \quad (6)$$

Step 6. Compare the new objective function value of each particle with its p_{best} and determine g_{best}.
Step 7. If the number of iteration reaches the maximum value, then move to step 8 otherwise move to step 4.
Step 8. The latest g_{best} is the solution to the problem.

2.7. Multi response optimization through multi-objective PSO

Multi-objective optimization problems deal with more than one objective function. Multi-objective optimization problems do not have one common solution, which is best with respect to the target. Pareto optimal solutions (POS) are a collection of optimal solutions, in which none of the solutions in the non-dominated solutions (Pareto optimal solutions) is absolutely better than any other. For perfect multi optimization of responses there are two tasks:
(i) To detect a set of non dominated solutions or POS

(ii) To pursue POS with a possible multiplicity of objectives and decision variable values using a higher-level of information.

Multi-objective PSO optimization algorithm uses the concept of domination with sorting and crowding distance approach in their search to find the best Pareto optimal solutions.

2.8. Concept of dominance

In this concept, solutions are compared over the other to obtain a dominant set of solutions over others. The outcome of dominance between two solutions 1 and 2 has three possibilities either one solution will dominate the other, or no solution dominates at all. In the present study, multi-objective optimization techniques use the continuously updated concept of domination. The current algorithm generates two solutions (*i* and *j*), which are compared for domination and check which one dominates the other from populations or not. At first, the primary solution from the population of the empty set was marked as R'. After that, all other i^{th} solutions were compared with all the solutions in set R' one at a time. If the i^{th} solution is dominated over R', then the corresponding solution is removed. This results in the elimination of non-member solution from the non-dominated solutions. If the i^{th} solution is dominated over R', then the solution is not neglected but is inserted in R'. In this way, the non-dominated solutions, called Pareto-optimal solutions, were generated. The following steps are used in this algorithm to search the non dominated set:

Step 1: Initialize R' = [1]. Set solution counter $i = 2$.

Step 2: Set j = l.

Step 3: Compare solution i with j from R' for domination.

Step 4: If i dominate j, delete the j^{th} member from R'. If $j < |R'|$, increment j by one and then go to Step 3. Otherwise, go to Step 5. Alternatively, if the j^{th} member of R' dominates i, increment i by one and then go to Step 2.

Step 5: Insert i in R'. If $i < N$, increment i by one and go to Step 2. Otherwise, stop and declare R' as the' non-dominated set.

2.9. Non-dominated sorting

In order to find the best Pareto front, sorting of non-dominated solutions are required. In this algorithm, the entire population are sorted as per the level of non-domination. The principal non-dominated solution is called Pareto-optimal fronts of level 1. To find the next level of the non-domination, the principal non-dominated set is deleted from the populations and then found the non-dominated solution of the remaining populations. The next non-dominated solution is called Pareto-optimal fronts of level 2. All non-dominated solutions of level 1 and level 2 are neglected from the populations and then new-dominated solutions found are called Pareto-optimal fronts of level 3. The procedure to find the sorting of the non-dominated set is:

Set all non dominated sets R_j, (j = 1, 2...) as empty sets. Set non-domination level counter j = 1.

Step 1 : Find the non-dominated set R′ of population R.

Step 2 : Update $R_j = R'$ and $R = R \setminus R'$

Step 3 : If $R \neq 0$, increment j by one and go to step 2. Otherwise, stop and declare all non-dominated sets R_i, for i = 1, 2 … j

2.10. Crowding distance method

To check for the non-dominated front from combined population P_t, the process starts with the principal non dominated front till the size of P_t is 2N. Comparison of solutions is done on the basis of non-dominated rank r_i and local distance d_i. If the two solutions have the same rank r_i, crowding distance approach is used to eliminate the solution having lower crowding distance d_i. The unoccupied space around the i is called crowding distance d_i The solidity of the solutions accompanying a particular solution i in the population is calculated by taking the average distance of two solutions on either side of solution i across each of the objectives. The following steps are used in this Algorithm to calculate the crowding distance:

Name the integer of solutions in F as l- $|F|$.

For each i in the set, first assign $d_i = 0$.

Step 1 : For each objective function m = 1, 2... M, sort the set in worse order of f_m or, End the sorted indices vector: I^m = sort (f_m ,>).

Step 2 : For m = 1, 2, . . . , M, assign a large distance to the boundary solutions, or $d_{I_1^m} = d_{I_j^m}$

=∞ and for all other solutions j = 2 to (l - 1), assign:

$$d_{I_j^m}=d_{I_j^m}+\frac{f_m^{(I_{j+1}^m)}-f_m^{(I_{j-1}^m)}}{f_m^{max}-f_m^{min}}$$

where,

I_j = solution index of the j[th] member in the sorted list;

f_m = values of objective on either side of solution I_j.

f_m^{max} = population-maximum of the m[th] objective function

f_m^{min} = population-minimum of the m[th] objective function

2.11.Finding Pareto optimal fronts by MOPSO

MOPSO is an integrated form of PSO which utilizes the best possible values for each particle for the comparison of non-dominated set effectively. All the personal's best values are compared in the entire population to Pareto optimal front. The following steps are used in this MOPSO algorithm:

Let R_t represent parent population at time t and S_t represent offspring population at time t.

Initially, $S_t = 0$ and a random population R_t of size N is created

Step 1: Combine parent and offspring population and create $P_t = R_t \cup S_t$

Classify the entire population ($P_t = N$) into various non dominated levels according to ascending level of dominance. Identify the different frontsF_i, i=1, 2, 3… 4 etc.

Step 2: Set new population $R_{t+1} = S_t$. Set a counter $i = 1$, until $|R(t+1)| + |F_i| < N$, perform $R_{t+1} = R_{t+1} \cup F_i$ and $i = i + 1$

Step 3: Perform the crowding procedure and include most extensively spread ($N - |R_{t+1}|$) solutions by using the crowding distance value in the sorted F_i to P_{t+1}

Step 4: Create offspring population S_{t+1} from R_{t+1} by:

1. Randomly choosing an individual g_{best} from the top 10% of the solutions.
2. Find p_{best} for each solution. Modify the velocity and position of each particle each by using:

$$v_{id}(t+1) = wv_{id}(t) + c_1 rand_1()\big(p_{id}(t) - x_{id}(t)\big) + c_2 rand_2()\big(p_{gd}(t) - x_{id}(t)\big)$$

$$x_{id}(t+1) = x_{id}(t) + v_{id}(t)$$

where $rand_1$ and $rand_2$ are random numbers between 0 to 1. If the current position is outside the boundaries, then current position is set to upper bound if $x_{id}(t+1) > upper\ bound$. Current position is set to lower bound if $x_{id}(t+1) < lower\ bound$.

Step 5: Perform steps 2 to 5 until stopping criteria met

2.12. Scanning electron micrograph, EDX and XRD analysis of WEDM machined Inconel 825

For microstructure analysis, a confirmation experiment was performed at optimum conditions. The etching process of the machined sample was carried out as suggested by Kumar et al. [24]. All measurement related to microstructure analysis was performed by a scanning electron microscope (JEOL, Model 6100, USA). The microstructure analysis included micro-cracks, craters, formation of the recast layer, and heat-affected zone on the machined surface of the work material. Energy Dispersive spectrograph (EDS) analysis was carried out to measure the elemental configuration of the machined surface. X-ray diffraction was carried out to study the phases of WEDM machined Inconel 825.

3. Results and discussion

RSM is a statistical method for analyzing the outcome of multiple input parameters on responses [25]. In this study, RSM was employed as a modeling tool for optimizing the operating parameters for the cutting of Inconel 825. Three significant parameters, i.e., material removal rate (MRR), surface roughness (SR), and wire wear ratio (WWR) were taken as output measures as these responses have a crucial effect on the industrial economy and surface integrity of Inconel 825. A total of 52 experiments were conducted on WEDM (Table 3), and results were analyzed by ANOVA.

3.1. Evaluation of design by FDS graph

The evaluation of the design was carried out by plotting the fraction design space (FDS) graph. FDS is a pre-experiment tool used after the design was built. FDS graph between the fraction of the design space with standard error mean for design is shown in Fig. 2. The purpose of evaluation graphs is to provide a visual check for the precision capability of a design. In the current design, the average error score of 0.406 was observed. A better design will have lower average error scores and more consistent error scores throughout the factor space. In the current design, FDS score of 0.90 was obtained, which means that the design used is stable and robust for the optimization experiment.

Model F-statistics of 33.67 implicits that the model is significant. The p-values <0.05 indicates that the linear (A, B, C, E) and interactive (AB, AC, AD, BE, CE) terms had a quite significant influence on MRR. The percentage contribution of A, B, C, E, AB, AC, AD, BE, CE for MRR is 45.19, 25.38, 8.18, 1.84, 3.12, 2.07, 1.09, 7.26, and 3.81%, respectively, which are calculated from Table 4 by dividing each variable sum of squares term by "model" sum of squares. The lack of fit is found to be not significant with a p-value of 0.9298. A predictive two-factor polynomial equation is established to describe the relationship between MRR and input variables as given by Eq. (7).

$$\begin{aligned}\text{MRR} = {} & 350.847 - 1.211 \times \text{Pulse on time} + \\ & 14.049 \times \text{Pulse off time} - 11.459 \times \\ & \text{Gap voltage} - 4.328 \times \text{Peak current} - \\ & 15.492 \times \text{Wire tension} + 4.868 \times \text{Wire feed} - \\ & 0.190 \times \text{Pulse on time} \times \text{Pulse off time} + \\ & 0.116 \times \text{Pulse on time} \times \text{Gap voltage} + \\ & 0.033 \times \text{Pulse on time} \times \text{Peak current} + \\ & 0.078 \times \text{Pulse on time} \times \text{Wire tension} - \\ & 0.113\text{Pulse on time} \times \text{Wire feed} + \\ & 0.007\ \text{Pulse off time} \times \text{Gap voltage} + 0.003 \times \\ & \text{Pulse off time} \times \text{Peak current} + 0.580 \times \\ & \text{Pulse off time} \times \text{Wire tension} - 0.081 \times \\ & \text{Pulse off time} \times \text{Wire feed} + 0.003 \times \\ & \text{Gap voltage} \times \text{Peak current} - 0.315 \times \\ & \text{Gap voltage} \times \text{Wire tension} + 0.098 \times \\ & \text{Gap voltage} \times \text{Wire feed} + 0.008 \times \\ & \text{Peak current} \times \text{Wire tension} + 0.041 \times \\ & \text{Peak current} \times \text{Wire feed} + 0.023 \times \\ & \text{Wire tension} \times \text{Wire feed} \ldots . \end{aligned} \quad (7)$$

3.2. Three dimensional plots of the interaction

T_{on} and IP exerted a maximum positive effect on MRR (Fig. 3-6). It is evident from the literature that at the high value of T_{on}, discharge energy, increases in the void, resulting in more melting and evaporation of material from the void, which in turn improves MRR [26].

Table 3. Central composite design with actual responses.

Run	T_{ON}	T_{OFF}	SV	IP	WT	WF	MRR	SR	WWR
1	0	0	0	0	0	-2	21.27	2.618	0.219
2	0	0	0	0	0	0	20.44	2.306	0.015
3	-1	-1	1	1	1	1	18.59	2.453	0.01347
4	1	-1	1	-1	1	1	27.79	2.967	0.0041
5	1	1	1	-1	-1	1	20.63	2.766	0.01908
6	1	-1	1	-1	-1	-1	27.69	2.867	0.01425
7	1	1	-1	1	-1	1	20.06	2.711	0.00337
8	0	0	0	0	0	0	21.97	2.673	0.13256
9	-1	1	-1	-1	-1	1	17.01	2.783	0.01848
10	-1	-1	1	1	-1	-1	21.34	2.844	0.15013
11	1	1	-1	1	1	-1	31.81	2.793	0.00976
12	-1	1	1	1	-1	1	16.17	2.716	0.05423
13	-1	1	-1	1	-1	-1	20.23	2.732	0.02236
14	1	-1	-1	-1	-1	1	27.63	2.678	0.00032
15	0	0	0	0	0	0	21.89	2.911	0.03677
16	0	0	0	0	0	0	20.41	2.875	0.03255
17	-1	-1	-1	1	-1	1	28.94	2.442	0.07354
18	2	0	0	0	0	0	31.25	3.32	0.01093
19	1	-1	-1	1	1	1	34.72	2.84	0.04773
20	0	-2	0	0	0	0	30.87	2.613	0.01845
21	0	2	0	0	0	0	17.19	2.667	0.01298
22	1	-1	1	1	1	-1	31.42	3.271	0.02028
23	-1	1	1	1	1	-1	18.55	2.514	0.00291
24	0	0	0	0	0	0	35.93	2.963	0.01573
25	1	1	-1	-1	1	1	28.95	3.299	0.15061
26	-1	-1	-1	-1	-1	-1	25.79	2.721	0.20167
27	-1	-1	1	-1	1	-1	19.92	2.489	0.14103
28	0	0	0	0	-2	0	24.09	2.767	0.00394
29	0	0	0	2	0	0	27.08	2.684	0.01292
30	-1	-1	1	-1	-1	1	20.21	2.681	0.02832
31	1	1	1	1	1	1	27.68	2.742	0.04154
32	0	0	0	0	2	0	26.05	2.792	0.00823
33	0	0	0	0	0	0	24.59	3.074	0.00545
34	-1	-1	-1	1	1	-1	25.47	2.622	0.01644
35	0	0	0	0	0	0	23.94	2.461	0.01049
36	0	0	-2	0	0	0	25.57	2.594	0.00661
37	1	1	1	1	-1	-1	33.28	2.892	0.12435
38	-1	1	-1	1	1	1	20.52	2.415	0.00404
39	-1	1	1	-1	-1	-1	16.7	2.521	0.04631
40	1	1	1	-1	1	-1	24.46	2.263	0.03279
41	-1	1	1	-1	1	1	16.71	2.318	0.01062
42	-1	-1	-1	-1	1	1	23.14	2.485	0.08701
43	0	0	2	0	0	0	19.61	2.734	0.01789
44	1	1	-1	-1	-1	-1	28.39	2.805	0.00616
45	1	-1	-1	-1	1	-1	34.56	2.827	0.00815
46	-2	0	0	0	0	0	14.7	2.844	0.03203
47	0	0	0	0	0	2	25.77	2.94	0.01582
48	1	-1	-1	1	-1	-1	36.14	2.833	0.02691
49	1	-1	1	1	-1	1	36.13	2.842	0.01832
50	0	0	0	0	0	0	29.48	2.853	0.00853
51	-1	1	-1	-1	1	-1	23.67	2.64	0.1215
52	0	0	0	-2	0	0	28.08	2.748	0.08998

It was observed from Fig. 4 that an increment in gap voltage resulted in a decrease in the MRR. The reason can be attributed to the fact that the high value of gap voltage results in increased among the two sparks and less discharge energy is produced between the gaps resulted in decreased MRR [27].

3.3. Analysis of variance for SR

The ANOVA for output response, SR, is summarized in Table 5. The Model F-statistics of 37.20 implicits that the model was significant. A, C, E, AB, AD, AE, AF, BC, BE, BF, CD, CE, DE, DF were significant terms for SR with their contribution percentage of 36.87, 0.837, 0.346, 3.016, 0.893, 5.083, 2.681, 11.173, 7.821, 4.357, 7.821, 0.212, 1.396, and 10.614 %, respectively, which are calculated from Table 5 by dividing each variable sum of squares term by "model" sum of squares. The p- value for lack-of fit value is 0.1642. It was observed from Fig. 7-10 and Fig. 11-14 that T_{on}, IP, and WF had an influential effect on surface roughness as compared to T_{off}, SV, and WT.

To describe the correlation between SR and the six process parameters, a predictive two-factor polynomial equation (Eq. (8), final equation in terms of actual factors) is established as follows:

$$SR = 12.284 - 0.197 \times Ton + 1.174 \times Toff + 0.166 \times SV - 0.195 \times IP - 1.939 \times WT - 2.053 \times WF - .006 \times Ton \times Toff - 0.000 \times Ton \times SV + 0.001 \times Ton \times IP + 0.026 \times Ton \times WT + 0.019 \times Ton \times WF - 0.006 \times Toff \times SV + 0.0002 \times Toff \times IP - 0.022 \times Toff \times WT + 0.016 \times Toff \times WF + 0.001 \times SV \times IP - 0.013 \times SV \times WT + 0.002 \times SV \times WF + 0.002 \times IP \times WT - 0.007 \times IP \times WF + 0.014 \times WT \times WF \quad (8)$$

3.4. Three dimensional plots of the interaction

With the increase of pulse-on time and peak current high frequency is generated in the gap and a pool of molten metal formed at high temperature that causes formations of gas bubbles. When gas bubbles explode, more material discharged from the surface cause's formation of deep and broader craters, which in turn increases the surface roughness [26, 28]. Surface roughness improved with an increase in pulse-off time. It was high at low value of pulse-off time and decreased with an increase in pulse-off time. This is because, with a too short pulse-off time, there is not sufficient time to clear the melted small particles from the gap between the wire electrode and work-piece, resulting in lower surface roughness [29].

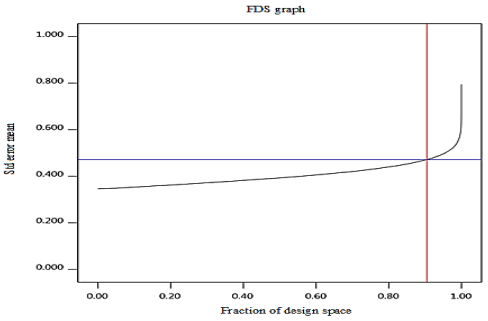

Fig. 2. FDS graph for the evaluation of design space.

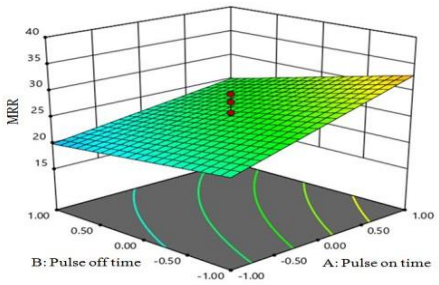

Fig. 3. Interactiv effects of pulse-on time and pulse-off time on MRR.

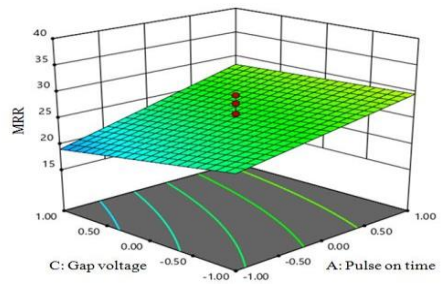

Fig. 4. Interactive effects of pulse-on time and gap voltage on MRR.

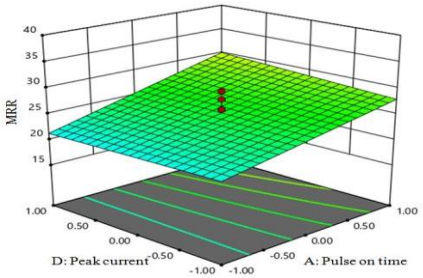

Fig. 5. Interactive effects of pulse-on time and peak current on MRR.

Table 4. Analysis of variance (ANOVA) for response surface model developed for MRR.

Source	Sum of squares	Df	Mean square	F value	p-value prob > F	
Model	1334.74	21	63.56	33.67	< 0.0001	Significant
A	603.23	1	603.23	319.54	< 0.0001	
B	338.79	1	338.79	179.46	< 0.0001	
C	109.23	1	109.23	57.86	< 0.0001	
D	7.04	1	7.04	3.73	0.0630	
E	24.66	1	24.66	13.06	0.0011	
F	3.69	1	3.69	1.95	0.1725	
AB	41.72	1	41.72	22.10	< 0.0001	
AC	27.71	1	27.71	14.68	0.0006	
AD	14.58	1	14.58	7.72	0.0093	
AE	0.79	1	0.79	0.42	0.5216	
AF	1.66	1	1.66	0.88	0.3564	
BC	0.27	1	0.27	0.15	0.7060	
BD	0.33	1	0.33	0.18	0.6779	
BE	96.95	1	96.95	51.36	< 0.0001	
BF	1.89	1	1.89	1.00	0.3248	
CD	0.54	1	0.54	0.28	0.5982	
CE	50.95	1	50.95	26.99	< 0.0001	
CF	4.98	1	4.98	2.64	0.1149	
DE	0.22	1	0.22	0.12	0.7326	
DF	5.48	1	5.48	2.90	0.0988	
EF	0.018	1	0.018	9.561E-003	0.9228	
Residual	56.63	30	1.89			
Lack of fit	33.79	23	1.47	0.45	0.9298	Not significant
Pure error	22.85	7	3.26			
Cor Total	1391.37	51				
Std. Dev.	1.37		R-squared	0.9593		
Mean	25.30		Adj R-squared	0.9308		
C.V. %	5.43		Pred R-squared	0.9137		
Press	120.04		Adeq precision	21.727		

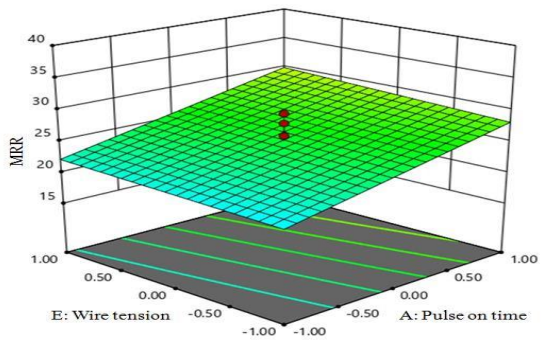

Fig. 6. Interactive effects of pulse-on time and wire tension on MRR.

Table 5. Analysis of variance (ANOVA) for response surface model developed for SR.

Source	Sum of squares	Df	Mean square	F value	p-value prob > F	
Model	1727.36	21	0.085	37.20	< 0.0001	Significant
A	637.26	1	637.26	288.17	< 0.0001	
B	2.06	1	2.06	0.93	0.3417	
C	14.74	1	14.74	6.67	0.0149	
D	5.99	1	5.99	2.71	0.1104	
E	20.14	1	20.14	9.11	0.0052	
F	3.14	1	3.14	1.42	0.2426	
AB	51.93	1	51.93	23.48	< 0.0001	
AC	0.046	1	0.046	0.021	0.8865	
AD	15.14	1	15.14	6.85	0.0138	
AE	87.77	1	87.77	39.69	< 0.0001	
AF	46.24	1	46.24	20.91	< 0.0001	
BC	188.11	1	188.11	85.06	< 0.0001	
BD	1.42	1	1.42	0.64	0.4295	
BE	134.48	1	134.48	60.81	< 0.0001	
BF	75.10	1	75.10	33.96	< 0.0001	
CD	137.81	1	137.81	62.32	< 0.0001	
CE	85.32	1	85.32	38.58	< 0.0001	
CF	3.67	1	3.67	1.66	0.2076	
DE	24.24	1	24.24	10.96	0.0024	
DF	186.30	1	186.30	84.25	< 0.0001	
EF	6.46	1	6.46	2.92	0.0978	
Residual	66.34	30	2.21			
Lack of fit	57.81	23	2.51	2.06	0.1642	Not significant
Pure error	8.53	7	1.22			
Cor Total	1793.71	51				
Std. Dev.	1.49		R-Squared	0.9630		
Mean	16.72		Adj R-Squared	0.9371		
C.V. %	8.89		Pred R-Squared	0.8491		
Press	270.62		Adeq Precision	35.840		

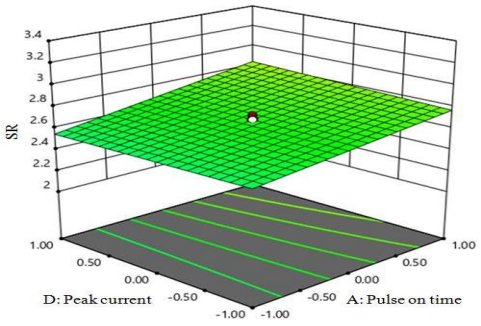

Fig.7. Three dimensional plot of combined effects of pulse-on time and peak current on SR.

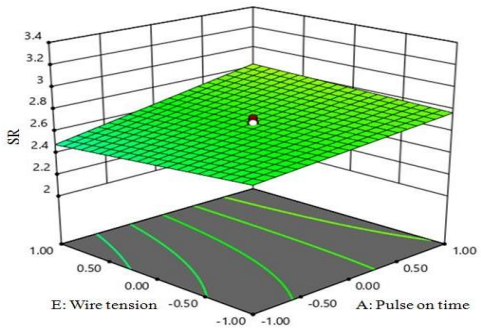

Fig. 8. Three dimensional plot of combined effects of pulse-on time and wire tension on SR.

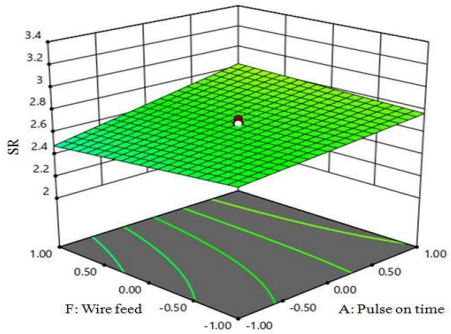

Fig. 9. Three dimensional plot of combined effects of pulse-on time and wire feed on SR.

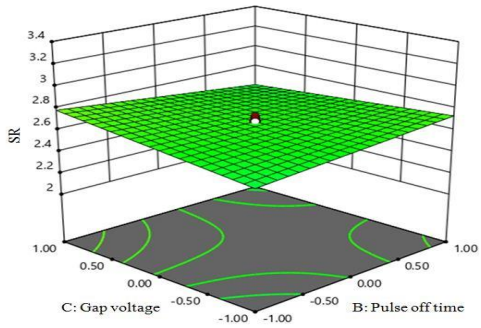

Fig. 10. Three dimensional plot of combined effects of pulse-off time and gap voltage on SR.

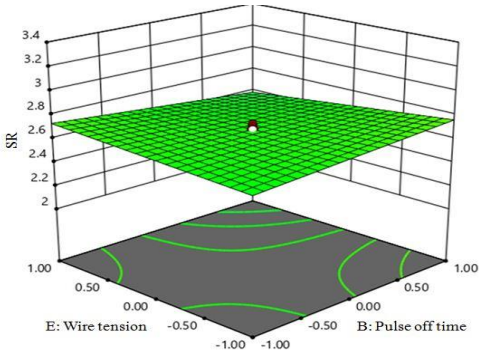

Fig. 11. Three dimensional plot of combined effects of pulse-off time and wire tension on SR.

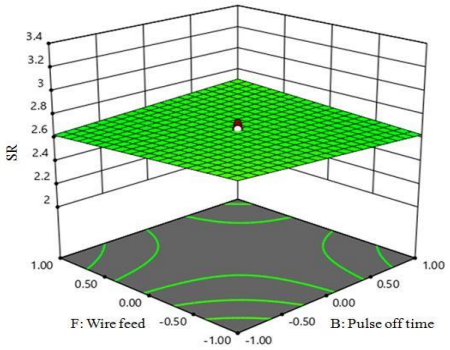

Fig. 12. Three dimensional plots of combined effects of pulse-off time and wire feed on SR.

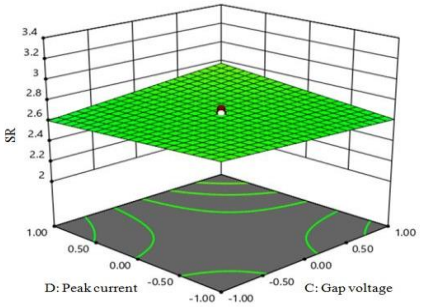

Fig. 13. Three dimensional plots of combined effects of gap voltage and peak current on SR.

3.5. Analysis of variance for WWR

The analysis of variance for output response WWR is summarized in Table 6.

The F-value of the model was 23.07 implicates that the model was significant. A, D, F, AB, AD, AE, AF, BD, BE, BF, CD, CE, CF, DE, DF, EF were significant model terms for WWR with their contribution percentage of 4.69, 3.85, 3.53, 19.51, 0.99, 2.79, 7.47, 0.96, 2.60, 2.98, 13.59, 8.38, 6.29, 7.97, 1.96, and 11.26 %, respectively, which were calculated from Table 6 by dividing each sum of squares term by "model" sum of squares.

A predictive two factor polynomial equation (Eq. (9), final equation in Terms of actual factors) is established to describe the correlation between WWR and the six process parameters as follows:

$$WWR = 22.221 - 0.204 \times Ton - 0.324 \times Toff - 0.001 \times SV - 0.020 \times IP - 0.234 \times WT - 0.616 \times WF + 0.002 \times Ton \times Toff + 0.00006 \times Ton \times SV + 0.0001 \times Ton \times IP + 0.003 \times Ton \times WT + 0.005 \times Ton \times WF - 0.0002 \times Toff \times SV - 0.0001 \times Toff \times IP + 0.002 \times Toff \times WT + 0.002 \times Toff \times WF + 0.0003 \times SV \times IP - 0.002 \times SV \times WT - 0.002 \times SV \times WF - 0.001 \times IP \times WT - 0.0005 \times IP \times WF + 0.012 \times WT \times WF \quad (9)$$

3.6. Three dimensional plots of the interaction

The results obtained from Fig. 15-18 and Fig. 19-20 show that WWR increases with the increase of Ton. It reaches its minimum value when the pulse-off time sets its maximum value, and SV sets its minimum value (Fig. 17-18). It is evident from the literature that an increase in input energy results in an increased wear rate of brass wire, which leads to wire breakage [30]. It has been observed that the increase in wire tension will reduce the vibrations of the wire and causes reduction in SR, which in turn improves the quality of the machined surface [31].

3.7.Multi-objective optimization using MOPSO

In this study, multi-objective optimization is carried out for finding the Pareto optimal fronts at different levels to maximize MRR and minimize SR in the first model and maximize MRR minimize WWR in the second model. MOPSO algorithm used the regression Eqs. (5-7) as the fitness function, and developed the two models, i.e., MRR and SR, and MRR and WWR.

Model 1: MRR and SR

The regression Eqs. (7 and 8) has been used as a fitness function and find the solution through multi-objective PSO. MOPSO algorithm resulted in 32 non-dominated set of solutions, as shown in Fig. 21.

The recommended optimum combination of input parameters, i.e., 109 machine unit T_{on}, 41 machine unit T_{off}, 51V SV, 138A IP, 10 machine unit WT and 8 m/min WF for which the values obtained for MRR and SR were 27.934 mm^2/min, 2.689µm, respectively (Table 7).

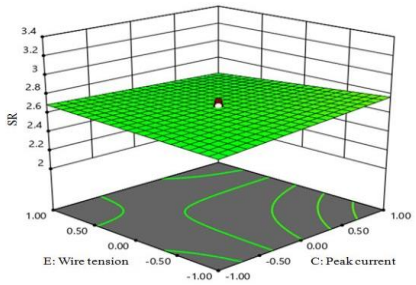

Fig. 14. Three dimensional plot of combined effects of peak current and wire tension on SR.

Table 6. Analysis of variance (ANOVA) for response surface model developed for WWR.

Source	Sum of Squares	Df	Mean Square	F Value	p-value Prob > F	
Model	21328.33	21	1015.63	23.07	< 0.0001	Significant
A	999.31	1	999.31	22.70	< 0.0001	
B	101.69	1	101.69	2.31	0.1390	
C	60.71	1	60.71	1.38	0.2495	
D	820.39	1	820.39	18.64	0.0002	
E	0.66	1	0.66	0.015	0.9035	
F	752.51	1	752.51	17.09	0.0003	
AB	4156.68	1	4156.68	94.43	< 0.0001	
AC	3.59	1	3.59	0.082	0.7770	
AD	211.26	1	211.26	4.80	0.0364	
AE	594.90	1	594.90	13.51	0.0009	
AF	1592.61	1	1592.61	36.18	< 0.0001	
BC	99.47	1	99.47	2.26	0.1432	
BD	204.74	1	204.74	4.65	0.0392	
BE	554.70	1	554.70	12.60	0.0013	
BF	636.62	1	636.62	14.46	0.0007	
CD	2895.66	1	2895.66	65.78	< 0.0001	
CE	1786.32	1	1786.32	40.58	< 0.0001	
CF	1341.37	1	1341.37	30.47	< 0.0001	
DE	1698.44	1	1698.44	38.58	< 0.0001	
DF	417.75	1	417.75	9.49	0.0044	
EF	2398.93	1	2398.93	54.50	< 0.0001	
Residual	1320.62	30	44.02			
lack of fit	1033.56	23	44.94	1.10	0.4856	Not significant
Pure error	287.07	7	41.01			
Cor total	22648.95	51				
Std. Dev.	6.63		R-Squared		0.9417	
Mean	81.13		Adj R-squared		0.9009	
C.V. %	8.18		Pred R-squared		0.8340	
Press	3759.52		Adeq precision		24.877	

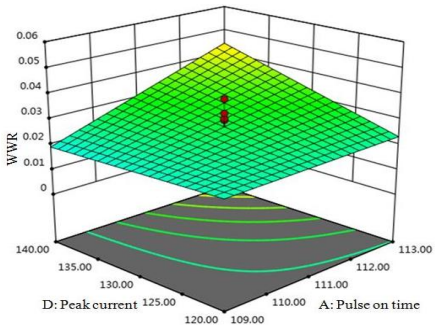

Fig. 15. Three dimensional interaction of pulse-on time and peak current on WWR.

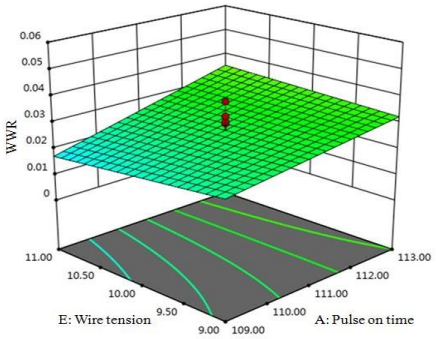

Fig. 16. Three dimensional interaction of pulse-on time and wire tension on WWR.

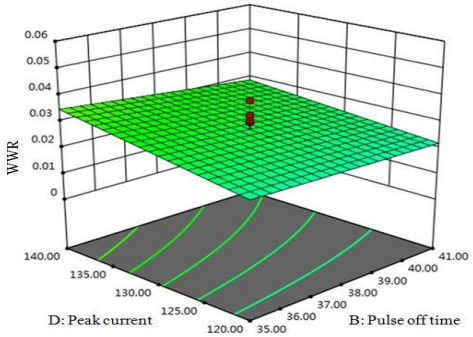

Fig. 17. Three dimensional interaction of pulse-off time and peak current on WWR.

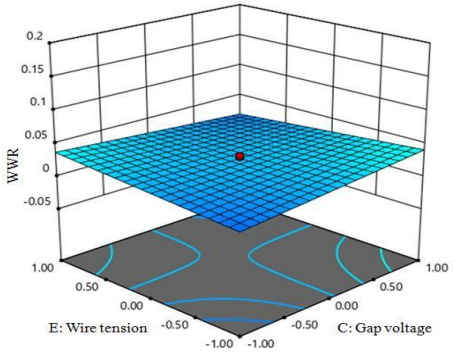

Fig. 18. Three dimensional interaction of gap voltage and wire tension on WWR.

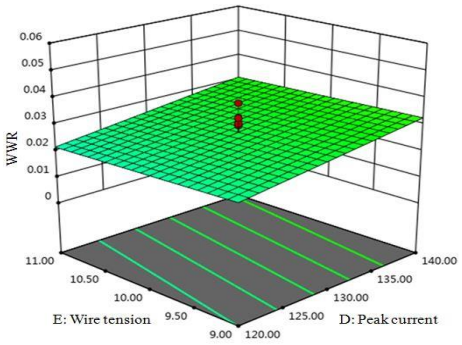

Fig. 19. Three dimensional interaction of peak current and wire tension on WWR.

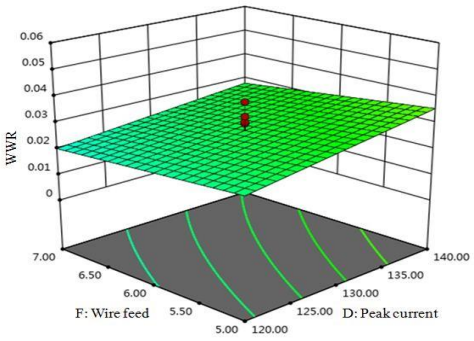

Fig. 20. Three dimensional interaction of peak current and wire feed on WWR.

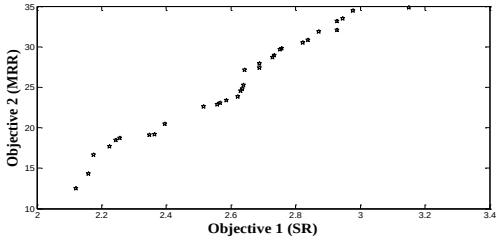

Fig. 21. Pareto optimal graph between MRR and SR.

At a high level of IP, the rate of discharge energy in the spark gap increases, which results in increased material removal rate. Due to rapid heating and quenching, the local temperature increases more than the melting point of the material resulting in the formation of cracks. Due to the emergence of intense and massive craters on the work surface, surface roughness gets increased, as observed from Fig. 21.

Model 2: MRR and WWR

The regression Eqs. (7 and 9) have been used as a fitness function and find the solution through multi-objective PSO. MOPSO algorithm resulted in 32 Pareto optimal solutions, as shown in Fig. 22.

The recommended optimum combination of input parameters, i.e., 108 machine unit T_{on}, 44 machine unit T_{off}, 48 V SV, 147 A IP, 8 machine unit WT, and 7 m/min WF for which the values obtained for MRR and WWR were 26.005 mm^2/min, 0.027, respectively (Table 8). At a low value of T_{on} and IP, MRR gets slightly enhanced; however, at a high value of wire tension, the WWR gets iimproved from 0.0265 to 0.073.
The confirmatory results obtained for model 2 show that there is a slightly improvement in MRR from 24.483 to 28.97 mm^2/min, as shown in Table 9.

3.8. Microstructure analysis

SEM, EDX, and XRD analysis were performed for workpiece surface and tool electrode surface machined with WEDM at an optimum combination of process parameters, i.e., 115 machine unit T_{on}, 42 machine unit T_{off}, 48V SV, 131A IP, 11 machine unit WT, and 7 m/min WF. The surface integrity study includes micro-cracks, craters, debris, pockmarks, heat-affected zone, and recast layer and transfer of the metal particles from the wire electrode to workpiece surface [32].
From the SEM micrograph (Fig. 23), it was observed that craters, pull-out materials, pockmarks, and recast layer were found on the surface of the work specimen due to rapid heating and cooling by the dielectric fluid [26, 33].
During machining with WEDM, melting and evaporation of work material occurred, and material gets removed in spherical shape causes crater and cracks formation. Crack size density depends on the discharge energy and thermal properties of the work material [34]. Because at high value of T_{on}, i.e., 115 machine unit high discharge energy transfers toward the work surface and more material melted and evaporated from the surface of the workpiece (Fig. 23).
From the SEM micrograph given in Fig. 24, it was observed that different craters and residual debris adhered to the surface of the tool electrode. Numbers of cracks, craters, and pockmarks were found on the tool surface because, at a high value of pulse on-time,a large amount of material migrated from the tool surface toward the work surface. Pulse-on time and peak current were found to be the most influencing parameters for the wire wear ratio.
SEM associated EDX analysis was used to investigate the presence of elements on the work surface other than base material (Fig. 25).

Table 7. Experimental observations for MRR and SR at optimized setting of input variables using MOPSO.

No.	A	B	C	D	E	F	MRR	SR
1	114	39	43	129	10	4	34.825	3.150
2	111	38	53	126	11	4	34.423	2.977
3	114	34	57	130	10	7	33.458	2.946
4	108	35	49	142	10	6	33.183	2.929
5	112	43	53	142	10	6	32.073	2.928
6	114	40	43	148	8	4	31.879	2.871
7	108	42	57	121	11	8	30.817	2.837
8	115	36	43	149	12	6	30.525	2.820
9	107	39	43	137	8	7	29.796	2.756
10	114	37	53	129	10	6	29.648	2.752
11	112	41	49	135	10	4	28.922	2.734
12	113	38	55	124	10	7	28.653	2.729
13	**109**	**41**	**51**	**138**	**10**	**8**	**27.934**	**2.689**
14	115	42	48	131	11	7	27.361	2.688
15	109	42	45	133	10	4	27.161	2.643
16	112	43	48	124	10	6	25.240	2.639
17	112	37	44	112	10	6	24.812	2.635
18	111	35	52	126	8	5	24.521	2.630
19	107	34	56	110	11	5	23.809	2.621
20	111	36	47	130	11	4	23.403	2.585
21	109	44	49	134	9	5	23.021	2.566
22	113	43	55	117	11	8	22.849	2.557
23	109	37	48	126	9	7	22.603	2.515
24	111	34	56	117	10	6	20.434	2.395
25	108	40	55	126	10	5	19.143	2.364
26	114	43	56	113	10	7	19.127	2.349
27	114	43	55	128	10	5	18.683	2.256
28	111	37	54	140	8	4	18.456	2.244
29	112	43	52	138	10	6	17.676	2.225
30	108	38	47	142	11	6	16.619	2.174
31	109	37	44	129	11	6	14.307	2.159
32	108	43	57	125	11	7	12.496	2.120

During the WEDM process some foreign elements Cr (chromium), Cu (copper), and Ni (nickel) were detected, which were migrated from the brass wire surface.

The highest peak in the spectrum shows the presence of more concentrated element like Cu than Cr and Ni in the specimen due to high melting and evaporation temperature (1084°C). The deposition of Cu and Ni elements was higher at the crater center than crater edges. Migration of these elements depends upon the value of T_{on} and SV. At a high level of T_{on} and SV, spark energy increases, which causes more melting and evaporation of material. Some residuals of the C (carbon), O (oxygen), and Cu elements were also observed on the tool electrode surface because of decomposition of dielectric, re-solidification of the wire electrode, and mixing of the debris at elevated temperature (Fig. 26).

From the EDX spectrum, it was observed that the Cu element is higher in proportion than Zn (Zinc) element in brass wire.

The debris that gets deposited in a compounded form on the work surface was examined by XRD analysis using X' Pert High score plus (Fig. 27).

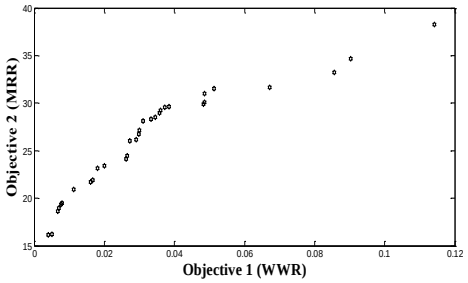

Fig. 22. Pareto optimal graph between MRR and WWR.

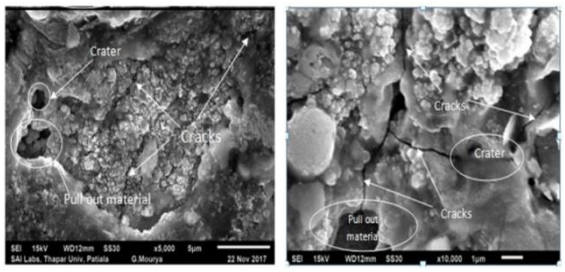

Fig. 23. SEM analysis of workpiece specimen cut under optimized condition, i.e., 109 machine unit T_{on}, 41 machine unit T_{off}, 51V SV, 138A IP, 10 machine unit WT, and 8 m/min WF.

Table 8. Experimental values of MRR and WWR at optimized setting of process parameters using MOPSO.

S.No.	A	B	C	D	E	F	MRR	WWR
1	108	37	54	110	12	7	38.243	0.114
2	107	44	42	114	10	4	34.694	0.090
3	113	41	44	119	9	8	33.198	0.085
4	111	38	6	139	9	4	31.644	0.067
5	111	42	46	115	10	7	31.544	0.051
6	114	42	54	141	10	5	30.969	0.048
7	112	37	47	129	12	7	30.052	0.048
8	115	41	48	140	12	5	29.888	0.048
9	111	41	57	142	9	7	29.594	0.038
10	115	39	52	123	11	7	29.559	0.037
11	113	37	44	130	10	7	29.238	0.036
12	107	40	44	126	11	5	28.955	0.035
13	108	34	45	128	11	4	28.485	0.034
14	112	39	47	142	8	8	28.323	0.033
15	108	32	58	116	12	5	28.106	0.031
16	108	37	42	150	10	8	27.153	0.030
17	108	40	53	139	10	7	26.770	0.029
18	111	38	56	149	10	6	26.175	0.029
19	**108**	**44**	**48**	**147**	**8**	**7**	**26.005**	**0.027**
20	109	35	49	126	9	7	24.483	0.026
21	115	42	58	117	9	6	24.156	0.026
22	109	34	54	117	11	6	23.393	0.020
23	111	34	46	113	11	7	23.123	0.018
24	111	39	46	133	11	7	21.873	0.016
25	109	33	49	129	11	7	21.728	0.016
26	108	33	50	132	8	7	20.907	0.011
27	111	42	43	136	10	4	19.509	0.008
28	115	43	58	134	10	6	19.328	0.007
29	110	35	56	126	12	6	18.964	0.007
30	107	40	48	137	8	7	18.601	0.006
31	112	39	56	131	10	7	16.242	0.005
32	108	40	44	136	10	8	16.161	0.004

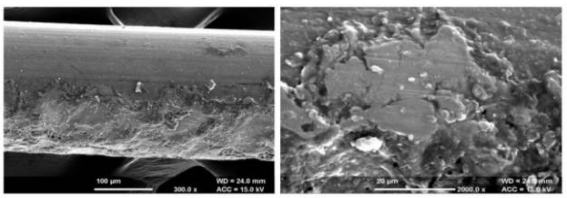

Fig. 24. SEM analysis of tool used for optimized cut, i.e., 109 machine unit T_{on}, 41 machine unit T_{off}, 51V SV, 138A IP, 10 machine unit WT, and 8 m/min WF.

Table 9. Confirmatory experiments for the multi-objective PSO.

Technique	Objective	Optimization parameters						Predicted Values	Confirmatory Results
		T_{on}	T_{off}	SV	IP	WT	WF		
MOPSO	Model 1	109	41	51	138	10	8	MRR 27.934 SR 2.689	MRR 31.687 SR 2.448
	Model 2	108	44	48	147	8	7	MRR 26.005 WWR 0.027	MRR 29.485 WWR 0.030

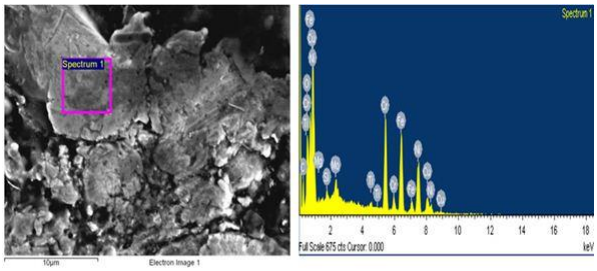

Fig. 25. EDX analysis of workpiece specimen cut under optimized condition, i.e., 109 machine unit T_{on}, 41 machine unit T_{off}, 51V SV, 138A IP, 10 machine unit WT, and 8 m/min WF.

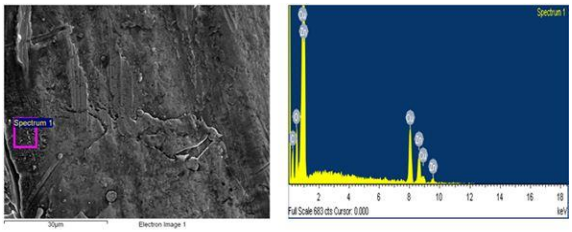

Fig. 26. EDX analysis of tool used for optimized run, i.e., 109 machine unit T_{on}, 41 machine unit T_{off}, 51V SV, 138A IP, 10 machine unit WT, and 8 m/min WF.

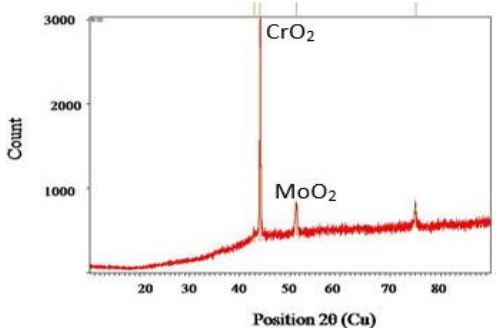

Fig. 27. XRD analysis for of workpiece specimen cut under optimized condition, i.e.,109 machine unit T_{on}, 41 machine unit T_{off}, 51V SV, 138A IP, 10 machineunit WT, and 8 m/min WF.

Under the action of the electric field, the electrolytic reaction takes place and Ti (titanium) atoms lose electrons and react with oxygen to form titanium oxides such as Ti_2O_3, TiO_2 and TiO, respectively. These oxides get attached on the surface of the workpiece and form oxidation film.

The oxidation film has poor thermal conductivity and a high melting point affecting the machining efficiency. It was observed from Fig. 27 that chromium dioxides (CrO_2) and molybdenum dioxides (MoO_2) were found as compounds formed on the surface of the specimen.

4. Conclusions

Multi-objective PSO was carried out to optimize the machining variables of WEDM. The following conclusions were made:

- The optimum setting obtained for MRR and SR was 109 machine unit T_{on}, 41 machine unit T_{off}, 51V SV, 138A IP, 10 machine unit WT, and 8 m/min WF for which the values obtained for MRR and SR were 27.934 mm^2/min, 2.689 µm, respectively.
- The optimum setting obtained for MRR and SR was 108 machine unit T_{on}, 4 machine unit T_{off}, 48 V SV, 147 A IP, 8 machine unit WT, and 7 m/min WF for which the values obtained for MRR and WWR were 26.005mm^2/min, 0.0265 respectively.
- It was concluded that T_{on}, SV, and IP have a significant positive effect on increasing MRR, while the increase in T_{off} resulted in decreased SR.
- SEM micrograph studies showed that a number of cracks, pockmarks, craters, and pulled-out material were found on the workpiece and wire electrode surface.

Declaration of conflicting interests

The author states that there is no conflict of interest.

References

[1] R. K. Palakudtewar and S. V. Gaikwad, "Dry Machining of Superalloys:

Difficulties and Remedies", *Int. J. Sci. Res.*, Vol. 3, pp. 277-282, (2014).

[2] G. Rajyalakshmi and P. Venkata Ramaiah, "Multiple process parameter optimization of wire electrical discharge machining on Inconel 825 using Taguchi grey relational analysis", *Int. J. Adv. Manuf. Tech.*, Vol. 69, pp. 1249-1262, (2013).

[3] G. R. Thellaputta, P.S. Chandra and C.S.P. Rao, "Machinability of Nickel Based Superalloys: A Review", *Mater. today: Proceed.*", Vol. 4, No. 2, pp. 3712-3721, (2017).

[4] E. Akca and A. Gursel, "A review on Superalloys and IN718 Nickel-Based Inconel Superalloy", *Period. Eng. Nat. Sci.*, Vol. 3, No. 1, pp. 15-27, (2013).

[5] M. Kumar and H. Singh, "Multi response optimization in wire electrical discharge machining of Inconel X-750 using Taguchi's technique and grey relational analysis", *Cogent Eng.*, Vol. 3, No. 1, pp. 1266123, (2016).

[6] A. Goswami and J. Kumar, "Investigation of surface integrity, material removal rate and wire wear ratio for WEDM of Nimonic 80A alloy using GRA and Taguchi method", *Int. J. Eng. Sci. Technol*., Vol. 17, No. 4, pp. 173-184, (2014).

[7] A. Thakur, A. Mohanty, S. Gangopadhyay and K. P. Maity, "Tool wear and chip characteristics during dry turning of Inconel 825", *Procedia Mater. Sci.*, Vol. 5, No. 1, pp. 2169-2177, (2014).

[8] G. Rajyalakshmi and P. Venkata Ramaiah, "A parametric optimization using Taguchi method: effect of WEDM parameters on surface roughness machining on Inconel 825", *Elixir. Mech. Eng.*, Vol. 43, No. 1, pp. 6669-6674, (2012).

[9] V. Aggarwal, S.S. Khangura and R.K. Garg, "Parametric modeling and optimization for wire electrical discharge machining of Inconel 718 using response surface methodology", *Int. J. Adv. Manuf. Technol.*, Vol. 79, No. 1-4, pp. 31-47, (2015).

[10] U. Çaydas and M. Ay, "WEDM cutting of Inconel 718 nickel-based superalloy: effects of cutting parameters on the cutting quality", *Mater. Technol.*, Vol. 50, No. 1, pp. 117–125, (2016).

[11] A. Goyal, "Investigation of material removal rate and surface roughness during wire electrical discharge machining (WEDM) of Inconel 625 super alloy by cryogenic treated tool electrode", *J. King Saud Univ. – Sci.*, Vol. 29, No. 4, pp. 528-535, (2017).

[12] G. Talla and S. Gangopadhyay, "Effect of impregnated powder materials on surface integrity aspects of Inconel 625 during electrical discharge machining", *Proc IMechE Part B: J. Eng. Manuf.*, Vol. 232, No. 7, (2016).

[13] S. Kumar, A.K. Dhingra and S. Kumar, "Parametric optimization of powder mixed electrical discharge machining for nickel based superalloy inconel-800 using response surface methodology", *Mech. Adv. Mater. Mod. Process.*, Vol. 3, No. 7, pp. 1-17, (2017).

[14] S. Bharti, S. Maheshwari and C. Sharma, "Multi-objective optimization of electric-discharge machining process using controlled elitist NSGA-II", *J. Mech. Sci. Technol.*, Vol. 26, No. 6, pp. 1875-1883, (2012).

[15] P. Saha, D. Tarafdar, K.S. Pal, P. Saha, K.A. Srivastava and K. Das, "Multi-objective optimization in wire-electro-discharge machining of TiC reinforced composite through Neuro-Genetic technique", *Appl. Soft Comp.*, Vol. 13, No. 4, pp. 2065–2074, (2013).

[16] S. A. Sonawane and M. L. Kulkarni, "Optimization of machining parameters of WEDM for Nimonic-75 alloy using principal component analysis integrated with Taguchi method", *J. King Saud Univ. Eng. Sci.*, Vol. 30, No. 3, (2018).

[17] K. Ishfaq, N.A. Mufti and M.P. Mughal, et al. "Investigation of wire electric discharge machining of stainless-clad steel for optimization of cutting speed", *Int. J. Adv. Manuf. Technol.*, Vol. 96, No. 5-8, pp. 1429. (2018).

[18] J. Kennedy and R. Eberhart, "Particle swarm optimization", *IEEE Int. Conf. Neur. Net.*, pp. 1942–1948, (1995).

[19] N. Baskar, P. Asokan, G. Prabhaharan and R. Saravanan, "Optimization of Machining Parameters for Milling Operations Using Non-Conventional Methods", *Int. J. Adv. Manuf. Technol.*, Vol. 25, No. 11, pp. 1078-1088, (2005).

[20] A. Majumder, P.K. Das, A. Majumder and M. Debnath, "An approach to optimize the EDM process parameters using desirability-based multi-objective PSO", *Prod. Manuf. Res.*, Vol. 2, No. 1, pp. 228-240, (2014).

[21] G. Rajyalakshmi, "Modeling and Multi-Objective Optimization of WEDM of Commercially Monel Super Alloy considering Multiple Users Preferences", *J. Pharm. Sci. Res.*, Vol. 8, No. 8, pp. 902-908, (2016).

[22] P. Sharma, D. Chakradhar and S. Narendranath, "Modeling and Optimization of WEDM performance attributes of Inconel 706 superalloy using RSM-based PSO approach", *The Ninth International Conference on Material Technologies and Modeling MMT-2016, At Ariel University*, Israel, Vol. 1, pp. 181-194, (2016).

[23] R. Chalisgaonkar and J. Kumar, "Multi-response optimization and modeling of trim cut WEDM operation of commercially pure titanium (CPTi) considering multiple user's preferences", *Int. J. Eng. Sci. Technol.*, Vol.18, No. 2, pp. 125-134, (2015).

[24] M. Kumar and H. Singh, "Optimization of process parameters of wire EDM for material removal rate using Taguchi technique", *Ind. J. Eng. Mater. Sci.*, Vol. 23, No. 1, pp. 223-230, (2016).

[25] D.P. Raykundaliya and A. Shanubhogue, "Comparison Study: Taguchi Methodology vis.-a-vis. Response Surface Methodology through a case study of accelerated failure in Spin-on-Filter", *Int. Adv. Res. J. Sci., Eng. Technol.*, Vol. 2, No. 3, pp. 1-5, (2015).

[26] T. Sultan, A. Kumar and R.D. Gupta, "Material removal rate, electrode wear rate, and surface roughness evaluation in die sinking EDM with hollow tool through response surface methodology", *Int. J. Manuf. Eng.* Vol. 2014, No. 8, pp. 259129, (2014).

[27] B. L. Skandesh, K.M. Mathew, R. Oyyaravelu and P. Kuppan, "Effect of Process Parameters on Material Removal Rate in µ-EDM of Magnesium Nano-Composite", *Int. Res. J. Eng. Technol.*, Vol. 3, No. 9, pp. 61-65, (2016).

[28] A. Giridharan and G. L. Samuel, "Analysis on the effect of discharge energy on machining characteristics of wire electrical discharge turning process", *J. Eng. Manuf.*, Vol. 230, No. 11, pp. 2064-2081, (2016).

[29] J. Singh, R. Singh and R. Kumar, "Review on Effects of Process Parameters in Wire Cut EDM and Wire Electrode Development", *Int. J. Innov. Res. Sci. Eng. Technol.*, Vol. 2, No. 11, pp. 701-706, (2016).

[30] R. Bobbili, V. Madhu and A.K. Gogia, "An experimental investigation of wire electrical discharge machining of hot-pressed boron carbide", *Def. Technol.*, Vol. 11, No. 4, pp. 344-349, (2015).

[31] S. V. Arikatla, M. K. Tamil and K. Arkanti, "Influence of Wire Feed Rate and Wire Tension in Wire Electrical Discharge Machining of Titanium Alloy" *Int. J. Innov. Res. Sci. Eng. Technol.*, Vol. 5, No. 1, pp. 274-281, (2016).

[32] Y. Shen, Y. Liu, H. Dong, K. Zhang, L. Lv, X. Zhang, X. Wu, C. Zheng and R. Ji, "Surface integrity of Inconel 718 in high-speed electrical discharge machining milling using air dielectric", *Int. J. Adv. Manu. Tech.*, Vol. 90, pp. 691-698, (2017).

[33] F. L. Amorim and W. L. Weingarten, "Die-sinking electrical discharge machining of a high-strength copper-based alloy for injection molds", *J. Braz. Soc. Mech. Sci. Eng.*, Vol. 26, No. 2, pp. 137–144, (2004).

[34] A. Kumar, V. Kumar and J. Kumar, "Surface crack density and recast layer thickness analysis in WEDM process through response surface methodology", *Mach. Sci. Technol.*, Vol. 20, No. 2, pp. 201-230, (2016).

How to cite this paper:

P. Kumar, M. Gupta, V. Kumar, " Multi-objective particle swarm optimization of WEDM process parameters for inconel 825", *J. Comput. Appl. Res. Mech. Eng.*, Vol. 10, No. 2, pp. 291-309, (2021).

DOI: 10.22061/jcarme.2019.4297.1518

URL: https://jcarme.sru.ac.ir/?_action=showPDF&article=1546